

This is the accepted manuscript made available via CHORUS. The article has been published as:

Two-color XUV plus near-IR multiphoton near-threshold ionization of the helium ion by circularly polarized light in the vicinity of the 3p resonance

A. N. Grum-Grzhimailo, N. Douguet, M. Meyer, and K. Bartschat

Phys. Rev. A **100**, 033404 — Published 6 September 2019

DOI: [10.1103/PhysRevA.100.033404](https://doi.org/10.1103/PhysRevA.100.033404)

Two-color XUV+NIR multi-photon near-threshold ionization of the helium ion by circularly polarized light in the vicinity of the 3p resonance

A. N. Grum-Grzhimailo¹, N. Douguet^{2,3}, M. Meyer⁴, and K. Bartschat⁵

¹*Skobeltsyn Institute of Nuclear Physics, Lomonosov Moscow State University, Moscow 119991, Russia*

²*Department of Physics, University of Central Florida, Orlando, FL 32816, USA*

³*Department of Physics, Kennesaw State University, Marietta, GA 30060, USA*

⁴*European XFEL GmbH, Holzkoppel 4, D-22869 Schenefeld, Germany and*

⁵*Department of Physics and Astronomy, Drake University, Des Moines, IA 50311, USA*

(Dated: August 12, 2019)

Two-color extreme-ultraviolet + near infrared (XUV + NIR) multi-photon ionization of the helium ion by circularly polarized light is studied in the vicinity of the 3p resonance. Combining the analysis of results obtained by solving the time-dependent Schrödinger equation and of the quasienergy spectrum of He^+ reveals the physical mechanisms that determine the photoelectron spectra and the variation of the circular dichroism as function of the NIR intensity.

I. INTRODUCTION

Ionization by strong circularly polarized fields at near-infrared (NIR) or visible light is an actively progressing field, both theoretically and experimentally, resulting, e.g., in high-order harmonic generation (HHG) with tunable polarization [1–4] and the production of a high degree of photoelectron spin polarization in multi-photon ionization [5]. Applications have been particularly concentrating on the study of chiral molecules [6–8] and of fundamental processes in strong-field ionization of atoms [9–11]. In addition, the production of circularly polarized extreme ultraviolet (XUV) photons at synchrotrons and HHG sources have produced a wealth of studies on dichroic processes in photoionization [12–15]. Processes with intense circularly polarized radiation at XUV frequencies currently attract much attention due to the availability of free-electron lasers (FELs) that can produce radiation with variable polarization in this frequency domain [16–18].

In a recent experiment, intense circularly polarized XUV and NIR laser pulses were combined to double ionize atomic helium [19]. Specifically, the first XUV photon with an energy of $\omega_{\text{XUV}} = 48.37 \text{ eV}$ from the FEL FERMI in Trieste (Italy) ionized atomic helium into the ionic ground state $\text{He}^+(1s)$. A second XUV photon with the same energy, in combination with a collinear NIR beam ($\omega_{\text{NIR}} = 1.58 \text{ eV}$), then further ionized the He^+ ion. The energy of 48.37 eV corresponds to the field-free $\text{He}^+(1s) \rightarrow \text{He}^+(3p)$ transition. With the moderate intensities of the photon beams, it is expected that ionization of $\text{He}^+(1s)$ proceeds predominantly via the $\text{He}^+(3p)$ state with subsequent ionization by absorption of four NIR photons.

The measured circular dichroism (CD) is defined as

$$\text{CD} = (P_+ - P_-)/(P_+ + P_-), \quad (1)$$

where P_+ and P_- are the angle-integrated photoemission probabilities after ionization by circularly polarized XUV and NIR pulses with the same (+) or opposite (−) helicity, respectively. An unexpected experimen-

tal result was a sharp decrease in the CD of the main photoelectron line from $0.98^{+0.02}_{-0.11}$ to $0.169^{+0.06}_{-0.10}$ when the peak intensity I_{NIR} of the NIR beam was only doubled, from $7.3 \times 10^{11} \text{ W/cm}^2$ to $1.4 \times 10^{12} \text{ W/cm}^2$, respectively. The experimental result was reproduced in [19] by numerically solving the time-dependent Schrödinger equation (TDSE), albeit with some intensity rescaling due to the use of shorter pulses with 22 fs full-width half-maximum (FWHM) intensity in the computations compared to $\approx 100 \text{ fs}$ in the experiment. The physical mechanism leading to the sharp decrease of the CD was suggested to be a helicity-dependent AC Stark shift of the $\text{He}^+(3p_{+1})$ state (here the subscript denotes the electron magnetic quantum number m) induced by the circularly polarized NIR field.

The present work represents a theoretical follow-up on the study reported in [19]. Specifically, we combine the numerical solution of the TDSE with an analysis of the quasienergy spectra, i.e., the position of the energy levels of He^+ in the presence of a monochromatic electromagnetic field. This approach allows us to further investigate the unexpected behavior of the CD and the corresponding photoelectron spectra in the near-threshold region.

Unless specified otherwise, atomic units are used throughout this manuscript.

II. NUMERICAL TREATMENT

The TDSE is solved starting from He^+ in its $1s$ ground state, which is then acted upon by electric fields of right-hand circularly polarized XUV radiation and right-hand ($\lambda = +1$) or left-hand ($\lambda = -1$) polarized NIR given by

$$\begin{aligned} \mathbf{E}(t) = & f_{\text{XUV}}(t) [F_{\text{XUV}}(\hat{\mathbf{x}} \cos \omega_{\text{XUV}}t + \hat{\mathbf{y}} \sin \omega_{\text{XUV}}t)] \\ & + f_{\text{NIR}}(t) [F_{\text{NIR}}(\hat{\mathbf{x}} \cos \omega_{\text{NIR}}t + \lambda \hat{\mathbf{y}} \sin \omega_{\text{NIR}}t)]. \end{aligned} \quad (2)$$

The z axis is chosen parallel to the radiation beams, i.e., the components of the electric field lie in the xy plane.

We take the pulse envelopes $f_{\text{XUV}}(t)$ and $f_{\text{NIR}}(t)$ as sine-square functions with a total of 40 NIR cycles and 1226

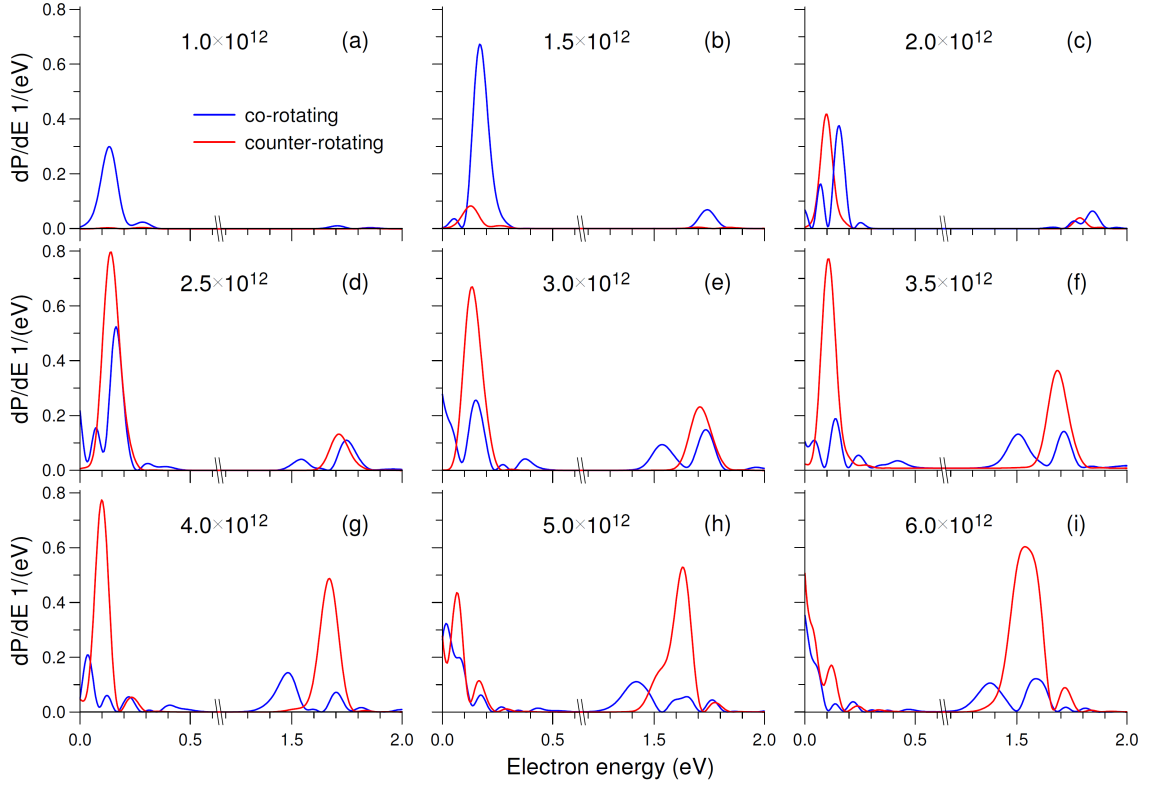


FIG. 1: Photoelectron spectra in the vicinity of the main photoelectron line **and the lowest ATI line** at different NIR peak intensities, as indicated in the panels (in W/cm^2). See text for the pulse parameters.

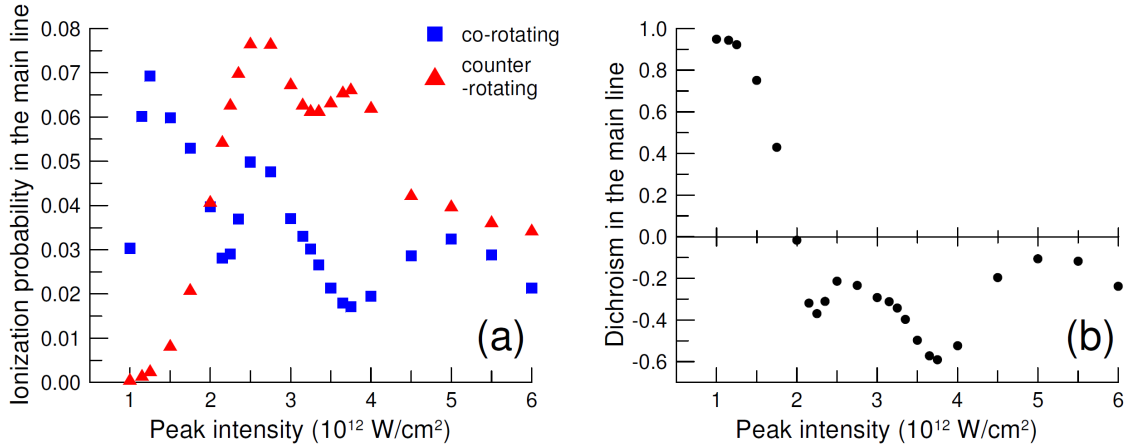


FIG. 2: Ionization probability in the main photoelectron line (a) and resulting CD (b) as function of I_{NIR} .

XUV cycles. With central frequencies corresponding to photon energies of 0.05811 a.u. (784 nm) and 1.7777 a.u. (26.5 nm), both envelopes yield full-width half-maximum (FWHM) intensities of approximately 40 fs. The fields start, end, and reach their maximum values at the same time, i.e., there is no delay between the XUV pulse that excites the He^+ ion and the NIR pulse that ionizes it further. F_{XUV} and F_{NIR} are the XUV and NIR field amplitudes, respectively, giving peak intensi-

ties (for the circularly polarized beams) of $I_{\text{XUV,NIR}} = 7.0 \times 10^{16} F_{\text{XUV,NIR}}^2 \text{ W}/\text{cm}^2$, where $F_{\text{XUV,NIR}}$ is given in atomic units. The carrier-envelope phases of the XUV and NIR fields are irrelevant for our case because of the large number of optical cycles in the XUV pulse. The XUV peak intensity is held fixed at $10^{13} \text{ W}/\text{cm}^2$, while the NIR peak intensity is varied between $10^{12} \text{ W}/\text{cm}^2$ and $6.0 \times 10^{12} \text{ W}/\text{cm}^2$, respectively. Details of the TDSE calculations of the photoelectron spectra may be found,

for example, in Ref. [20]. In the present TDSE calculations, performed in the velocity gauge, the space-time grid was characterized by a spatial step of $h = 0.015 a_0$ (where a_0 denotes the Bohr radius), a global grid radius of $r_{max} = 1450 a_0$, a minimum time step of $dt = 0.005$ atomic units (1 au = 24.19 attoseconds) for the highest intensity, slightly larger dt at lower intensities, and the maximum number of partial waves used for the highest intensity is $\ell_{max} = 55$. These values of the parameters provide converged results in the entire domain of electron energies and I_{NIR} considered for the selected pulse duration.

III. NUMERICAL RESULTS: SPECTRA AND CIRCULAR DICHROISM

Figure 1 shows the main line of the photoelectron spectra produced in the $\omega_{XUV} + 4\omega_{NIR}$ process for co- and counter-rotating fields at different I_{NIR} . The CD of this line is obtained after integrating the respective spectra for ejected-electron energies up to 0.5 eV. The energy dependence exhibited in the various panels is quite complex, both in the position and the value of several local maxima.

Figure 1 also exhibits the ejected-electron spectrum covering the lowest above-threshold ionization (ATI) peaks at electron energies above 1.2 eV. The ATI structure is equally complex at large I_{NIR} , developing from a dominating peak for the co-rotating case at 1.5×10^{12} W/cm² to several reduced peaks for this case and a strong asymmetric peak for counter-rotating pulses at 5.0×10^{12} W/cm², which reaches here similar intensities as the main line. There is a clear gap between the main line and the first ATI peaks, which makes it possible to unambiguously integrate over the electron energies that form these lines. The energy-integrated line intensities obtained in this way and the resulting CD for the main line are displayed in Fig. 2 as a function of I_{NIR} . As expected from Fig. 1, the curves show significant structure. With increasing I_{NIR} , the CD falls rapidly from the low-intensity value of ≈ 0.96 , changes sign around 2.0×10^{12} W/cm², and then varies in a nontrivial way at higher I_{NIR} .

IV. DISCUSSION

The remainder of this manuscript is devoted to the discussion of the predicted lines, in particular the CD associated with the main line. We first introduce the quasienergy spectra and then use them to interpret the TDSE results.

A. Quasienergy Spectra

The spectra of the dressed states and the dynamic Stark shifts have been efficiently used for a long time to explain structures in the photoelectron spectra of atoms and molecules exposed to high-intensity electric fields. Many references can be found in early reviews such as [21–24] and books [25–27], while more recent developments are described, e.g., in [28–30]. The importance of the time-dependent nature of the problem has been repeatedly emphasized, because a wealth of resonance conditions can be satisfied for many atomic levels during the laser pulse. As a result, transient dynamic (“Freeman”) resonances [31] may appear in the photoelectron spectra. Nevertheless, given the relatively long length of the pulses of interest for the present work (40 fs FWHM) compared to the period of an optical cycle of the NIR radiation, one may expect valuable information from the quasienergy spectra, even though they are calculated with a monochromatic field, i.e., effectively an infinite pulse length.

In order to bring a deeper insight into the physics of the phenomenon, Fig. 3 exhibits the essential part of the quasienergy spectrum of He⁺. Specifically, it is a map of the real parts of the quasienergies (energies of the “dressed states”), which are obtained by solving the Schrödinger equation for the target (here He⁺) in the presence of a circularly polarized monochromatic NIR field. The ponderomotive shifts due to the XUV field are negligible for the peak intensity I_{XUV} discussed here. This allows us to avoid the solution of the full two-color Floquet eigenvalue problem [32]. We generated the quasienergy spectra using the code STRFLO [33] in the non-perturbative regime by solving the Floquet equations. The calculations were performed in the velocity gauge with a radial basis of up to 80 Sturmian functions in each partial wave, the latter ranging up to $l = 20$. Harmonic components with absolute values of the photon index up to $|N_M| = 18$ were included. Different rotation angles in the complex scaling of the radial variable were applied to check the convergence. Our calculations confirm that the quasienergy spectrum is quite complex even for one-electron systems [34–36].

Figures 3(a,c) and 3(b,d) correspond to the counter-rotating and co-rotating NIR and XUV fields, respectively. While the upper and lower panels contain similar information for the two cases, they are presented with different scales and styles that are convenient for various aspects of the discussion below. As mentioned above, although the quasienergy spectra do not accurately describe the case of finite pulses, we believe that considering these spectra reveals the major aspects of the ionization mechanism.

At the lowest intensities, the curves in Figs. 3(a,b) are labeled by their adiabatic zero-NIR-field hydrogen-like configuration. For example, $3p(+1,0)$ is the state resonantly excited after the absorption of the (second) XUV photon from the 1s ground state of the ion. The

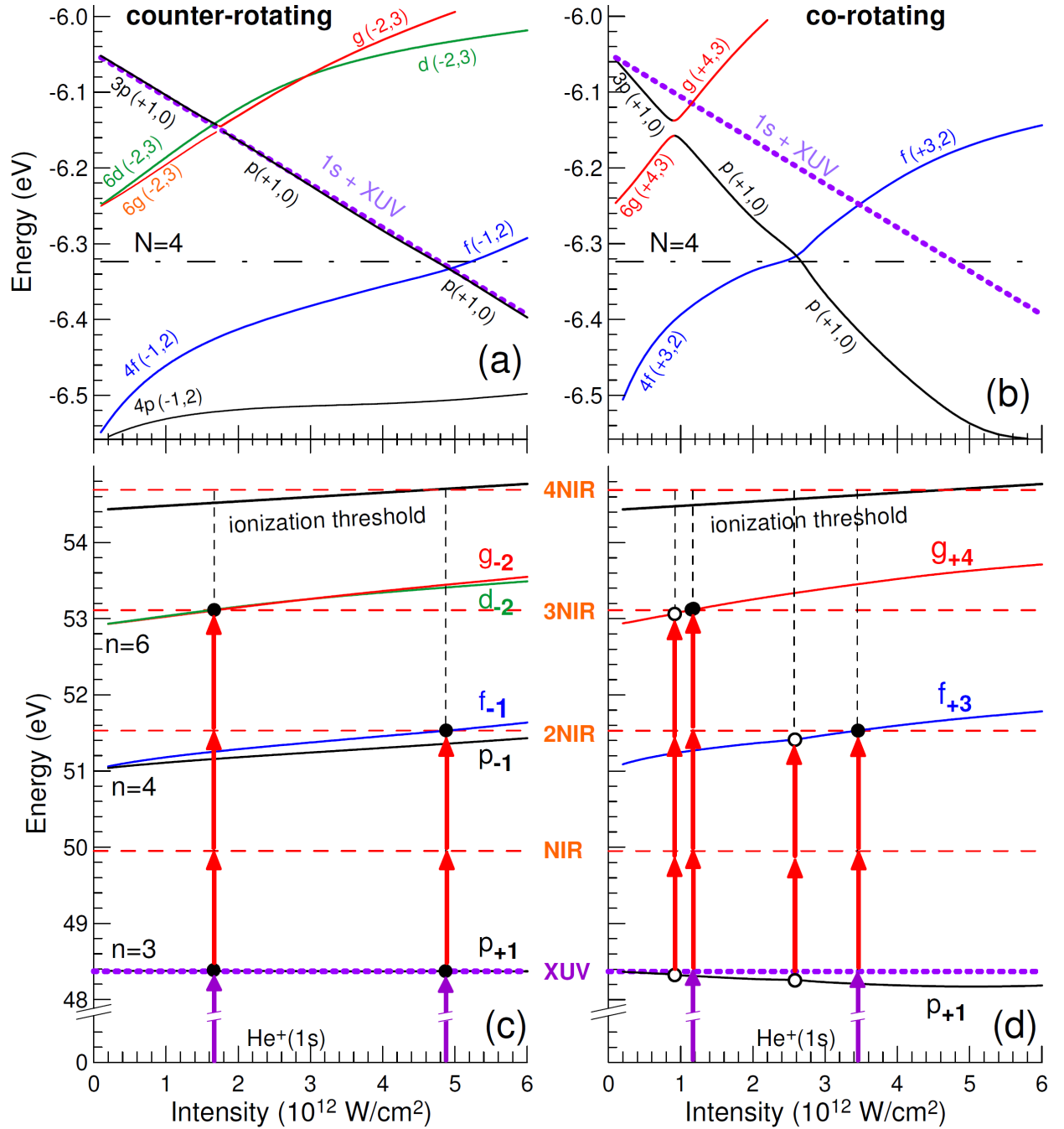


FIG. 3: Quasienergy spectra of He^+ for counter-rotating (a,c) and co-rotating (b,d) XUV and NIR fields. The horizontal line marked by $N = 4$ shows the border between energy-allowed (above the line) and energy-forbidden (below the line) four-photon ionization by the NIR field. Zero energy corresponds to the ionization threshold in (a) and (b), while the energy in (c) and (d) is counted from the ionic ground state. Solid circles mark resonantly coupled quasienergy levels with the XUV photon participating, while open circles mark couplings due to NIR photons only. The dashed vertical lines indicate the ionization paths. See text for further explanations.

dotted line in each panel of Fig. 3 shows the energy of the $\text{He}^+(1s)$ dressed state including the XUV energy (48.37 eV). Its fast decrease with increasing NIR intensity in panels 3(a,b) reflects the ponderomotive shift of the ionization threshold of He^+ .

Due to the axial symmetry with respect to the propagation direction of the beams (recall that this is our z axis of quantization) and the lack of spherical symmetry of the “atom+field” system, the only rigorously conserved quantum number in our nonrelativistic treat-

ment is the projection of the total angular momentum of the system [$\text{He}^+ + N$ NIR photons] on the z axis. Therefore, we only present the quasienergy spectra of the levels with $m = 1 + \lambda N$, where N is the number of absorbed photons. In Figs. 3(a,b), zero energy corresponds to the ionization threshold. The values of m and N are indicated, respectively, in parentheses after the configuration, which is presented by the leading symmetry. Furthermore, in order to facilitate the discussion below, the quasienergy curves of the dressed excited He^+ states are shifted down by the energy of the N NIR photons to the interval containing the $3p_{+1}(+1, 0)$ state. As an example, $6g(-2, 3)$ is the relevant state with principal quantum number $n = 6$ after absorption of three photons with negative helicity from the $3p_{+1}(+1, 0)$ state (Fig. 3(a)). Similarly, $4f(+3, 2)$ is the result after absorption of two photons with positive helicity (Fig. 3(b)). Note that the two dressed states involved switch their configuration character at an avoided crossing: $3p(+1, 0)$ (or $p(+1, 0)$) with $6g(-2, 3)$ (or $g(-2, 3)$) in Fig. 3(a) and with $6g(+4, 3)$ (or $g(+4, 3)$) in Fig. 3(b). This is additionally indicated in Figs. 3(a,b) by changing the color (gray scale) of the curves after the avoided crossing.

In this representation, the crossings of the “ $1s+\text{XUV}$ ” line with other curves correspond to multi-photon XUV + NIR resonances. Specifically, the resonance condition is met at certain intensities of the NIR field when $\omega_{\text{XUV}} + N\omega_{\text{NIR}} = E_k - E_{1s}$, where E_k is the quasienergy of the level k , E_{1s} the energy of the dressed ground $\text{He}^+(1s)$ state, and N the number of NIR photons. These resonances are marked in Figs. 3(c,d) by filled circles. Looking at the counter-rotating case, Figs. 3(a,c), the quasienergies are such that there is an XUV + three-photon resonance between the $n = 3$ and $n = 6$ levels at an NIR intensity of about $1.65 \times 10^{12} \text{ W/cm}^2$, while there is an XUV + two-photon resonance between the $n = 3$ and $n = 4$ levels around $4.85 \times 10^{12} \text{ W/cm}^2$. Additional $N\omega_{\text{NIR}}$ resonances that are close to the $\omega_{\text{XUV}} + N\omega_{\text{NIR}}$ resonances are indicated by open circles in Fig. 3(d). The former may also contribute significantly to the ionization process [37].

Remarkably, for the counter-rotating fields shown in Figs. 3(a,c), the quasienergy of the $\text{He}^+(p_{+1})$ state practically overlaps with the “ $1s+\text{XUV}$ ” quasienergy over the entire intensity range of interest. In other words, the dressed $\text{He}^+(1s)$ and $\text{He}^+(3p_{+1})$ states are in resonance with the XUV field independent of I_{NIR} . Consequently, the difference in the energy levels, which is shown in the “XUV” line of Figs. 3(c), is very close to the $\text{He}^+(p_{+1})$ energy.

The situation is very different for the co-rotating fields (see Figs. 3(b,d)), for which the quasienergy of the $\text{He}^+(p_{+1})$ dressed state decreases with respect to the “ $1s+\text{XUV}$ ” line and, therefore, goes out of resonance with the XUV field. The different behavior of levels with $m \neq 0$ was predicted already a long time ago within lowest-order perturbation theory due to the vector component of the polarizability, which has opposite signs

for $\pm m$ magnetic sublevels in fields of counter- and co-rotating helicity [26, 38, 39]. As we show below, in the non-perturbative regime this unlike behavior can lead to qualitative differences in the XUV + NIR ionization by co- and counter-rotating fields in the region of an intermediate resonance with nonzero orbital angular momentum.

It is important to recall that the intensity of the constant-amplitude field in the quasienergy calculation is not equivalent to the peak intensity of the finite radiation pulse. To compare the quasienergy and the TDSE results, therefore, the intensity in the former case generally should be reduced. In the present study, no rescaling of the intensity to simulate the longer pulses employed in [19] was applied in the TDSE calculations.

B. Interpretation of the TDSE predictions

Bearing the above issues in mind, we can now qualitatively explain the physics behind the main features of the photoelectron spectra displayed in Fig. 1, as well as the total probability and the CD results depicted in Fig. 2. As discussed in [19] and seen again in Figs. 1(a,b), at the lowest NIR intensities the co-rotating field can much more efficiently ionize the $\text{He}^+(3p_{+1})$ state compared to the counter-rotating field. Consequently, $\text{CD} \approx 1$, as exhibited in Fig. 2(b).

Below we consider subsequently ionization by counter-rotating fields, Fig. 3(a,c), and co-rotating fields, Fig. 3(b,d). Comparing them provide insight into the energy dependence of the CD.

The rapid enhancement of the counter-rotating main line with increasing I_{NIR} until a first saturation around $I_{\text{NIR}} = 2.5 \times 10^{12} \text{ W/cm}^2$ is explained by the stable resonance conditions for the XUV light, which is tuned to the $\text{He}^+(1s) - \text{He}^+(p_{+1})$ transition independent of I_{NIR} and further enforced by the $3\omega_{\text{NIR}}$ resonance between the dressed p_{+1} and d_{-2}, g_{-2} states; see Figs. 3(a,c). The second maximum in Fig. 2(a) is due to the $2\omega_{\text{NIR}}$ resonance between the dressed p_{+1} and f_{-1} states. At higher intensities the line begins to move below the threshold, due the ponderomotive shift of the ionization potential, as seen in Figs. 1(h,i). Correspondingly, the intensity of the line decreases, although its low-energy wing already excites Rydberg states of He^+ . This, in turn, causes an increase of the ionization probability at the threshold and a low-energy shoulder in the ATI peak, which is clearly seen in Fig. 1(h).

The behavior of the main line for the co-rotating fields is more intricate, reflecting a more complicated interplay of the dressed levels displayed in Figs. 3(b,d). Increasing the NIR intensity first leads to an enhancement of the main line (see Figs. 1(b), 2(a)). This is reinforced by the $3\omega_{\text{NIR}}$ resonance between the p_{+1} and g_{+4} dressed states, even though the XUV is no longer in perfect match with p_{+1} . When I_{NIR} is further increased, the weakening of the main line around $I_{\text{NIR}} = 2 \times 10^{12} \text{ W/cm}^2$ (see

Figs. 1(c), 2(a)) is caused by the further deviation of the p_{+1} level from the $1s - 3p_{+1}$ resonance. Combined with the growing intensity of the photoelectron line in the latter case, it is this effect, which is absent for the counter-rotating fields, that causes such a rapid drop and even a sign change of the dichroism with increasing I_{NIR} (Fig. 2(b)), exactly as observed experimentally [19].

In parallel, the photoelectron line develops into a pronounced doublet shown in Figs. 1(c,d). The high-energy component is due to direct $4\omega_{\text{NIR}}$ ionization while we attribute the low-energy component to the resonantly $p_{+1} - g_{+4}$ $3\omega_{\text{NIR}}$ enhanced ionization. This splitting is clearly reflected in the quasienergy spectrum shown in Fig. 3(b), where a splitting of about 0.1 eV develops between the “1s+XUV” and the p_{+1} curves. Part of the low-energy component moves below the ionization threshold (see Figs. 1(d,e)), which is reinforced by resonances associated with high-lying Rydberg states of He^+ . This is reflected onto the ATI line in the form of a doublet, as seen in Figs. 1(e-i). Only the higher-energy component is a true ATI peak, very close in energy with the ATI peak for the counter-rotating fields. The lower-energy component is actually not due to ATI, but rather represents the main photoelectron line from the resonant $\omega_{\text{XUV}} + 5\omega_{\text{NIR}}$ ionization. Thus, we observe the remarkable case of almost overlapping electron lines, originating from direct ionization and ATI, produced by beams of the same energy but different helicity. At NIR intensities of $2.5 - 3.0 \times 10^{12} \text{ W/cm}^2$ the line is enhanced by the $2\omega_{\text{NIR}}$ $p_{+1} - f_{+3}$ and $\text{XUV} + 2\omega_{\text{NIR}}$ $p_{+1} - f_{+3}$ resonances. As seen in Fig. 2, this causes a pronounced maximum in the ionization probability for the co-rotating fields and, consequently, a broad structure in the CD.

The decreasing absolute value of the CD above $4 \times 10^{12} \text{ W/cm}^2$ is related to the counter-rotating main line moving below the ionization threshold, in parallel with an enhancement of the main line from co-rotating fields just at the threshold due to the $2\omega_{\text{NIR}}$ $p_{+1} - f_{+3}$ resonance. Above $I_{\text{NIR}} \approx 4.5 \times 10^{12} \text{ W/cm}^2$, a substantial part of the main line shifts below threshold, and hence its CD is no longer clearly defined.

V. SUMMARY AND CONCLUSIONS

We studied two-color XUV + NIR multi-photon near-threshold ionization of $\text{He}^+(1s)$ by circularly polarized

light, when the energy of the XUV photons is in resonance with the field-free $1s - 3p$ transition. The combined analysis of the TDSE results and of the quasienergy level spectrum showed that a different reaction of the magnetic sublevel $3p_{+1}$ to light fields of the same or opposite helicities plays a key role in the experimentally observed sharp decrease of the circular dichroism with increasing NIR intensity. Resonance transitions between quasienergy levels of He^+ and their evolution with the NIR intensity explain the main features of the observed photoelectron spectra and the circular dichroism.

A more detailed explanation of the fine-structure features and their relative intensities in the photoelectron spectra obtained by solving the TDSE needs a comprehensive analysis with accounting for the pulse envelope and the time-dependent populations of Rydberg He^+ states. Furthermore, the present results call for a thorough study of the quasienergy spectra of polarized states in strong circularly polarized fields. On the experimental side, a crucial test of the proposed main mechanism governing the sharp drop of the CD with increasing I_{NIR} would be to perform measurements with different time delays between the XUV and NIR pulses.

Acknowledgments

The work of N.D. and K.B. was supported by the United States National Science Foundation under grants Nos. PHY-1403245 and PHY-1803844, as well as the XSEDE allocation PHY-090031. Most of the calculations were performed on Comet at the San Diego Supercomputer Center. M.M. acknowledges support by the Deutsche Forschungsgemeinschaft (DFG) under Grant No. SFB925/A1. The authors are grateful to E.V. Gryzlova for valuable discussions.

-
- [1] A. Fleischer, O. Kfir, T. Diskin, P. Sidorenko, and O. Cohen, *Nature Photonics* **8** (2014) 543.
 - [2] A. Ferré, C. Handschin, M. Dumergue, F. Burgy, A. Comby, D. Descamps, B. Fabre, G. A. Garcia, R. Géneaux, L. Merceron, E. Mével, L. Nahon, S. Petit, B. Pons, D. Staedter, S. Weber, T. Ruchon, V. Blanchet, and Y. Mairesse, *Nature Photonics* **9** (2015) 93.
 - [3] O. Kfir, P. Grychtol, E. Turgut, R. Knut, D. Zusin, D. Popmintchev, T. Popmintchev, H. Nembach, J. M. Shaw, A. Fleischer, H. Kapteyn, M. Murnane, and O. Cohen, *Nature Photonics* **9** (2015) 99.
 - [4] K. M. Dorney, J. L. Ellis, C. Hernández-García, D. D. Hickstein, C. A. Mancuso, N. Brooks, T. Fan, G. Fan, D. Zusin, C. Gentry, P. Grychtol, H. C. Kapteyn, and M. M. Murnane, *Phys. Rev. Lett.* **119** (2017) 063201.
 - [5] M.-M. Liu, Y. Shao, M. Han, P. Ge, Y. Deng, C. Wu,

- Q. Gong, and Y. Liu, *Phys. Rev. Lett.* **120** (2018) 043201.
- [6] C. Lux, A. Senftleben, C. Sarpe, M. Wollenhaupt, and T. Baumert, *J. Phys. B* **49** (2016) 02LT01.
- [7] M. H. M. Janssen and I. Powis, *Phys. Chem. Chem. Phys.* **16** (2014) 856.
- [8] R. E. Goetz, C. P. Koch, and L. Greenman, *Phys. Rev. Lett.* **122** (2019) 013204.
- [9] I. Barth and O. Smirnova, *Phys. Rev. A* **84** (2011) 063415.
- [10] L. Torlina, F. Morales, J. Kaushal, I. Ivanov, A. Kheifets, A. Zielinski, A. Scrinzi, H. G. Muller, S. Sukiasyan, M. Ivanov, and O. Smirnova, *Nature Physics* **11** (2015) 503.
- [11] S. Eckart, M. Kunitski, M. Richter, A. Hartung, J. Rist, F. Trinter, K. Fehre, N. Schlott, K. Henrichs, L. Ph. H. Schmidt, T. Jahnke, M. Schöffler, K. Liu, I. Barth, J. Kaushal, F. Morales, M. Ivanov, O. Smirnova, and R. Dörner, *Nature Physics* **14** (2018) 701.
- [12] G. A. Garcia, L. Nahon, S. Daly, and I. Powis, *Nature Communications* **4** (2013) 2132.
- [13] M. Pitzer, M. Kunitski, A. S. Johnson, T. Jahnke, H. Sann, F. Sturm, L. Ph. H. Schmidt, H. Schmidt-Böcking, R. Dörner, J. Stohner, J. Kiedrowski, M. Reggelin, S. Marquardt, A. Schießer, R. Berger, M. S. Schöffler, *Science* **341** (2013) 1096.
- [14] L. Nahon, G. A. Garcia, and I. Powis, *J. Electron Spec. Rel. Phenom.* **204** (2015) 322.
- [15] A. Comby, E. Bloch, C. M. M. Bond, D. Descamps, J. Miles, S. Petit, S. Rozen, J. B. Greenwood, V. Blanchet, and Y. Mairesse, *Nature Communications* **9** (2018) 5212.
- [16] T. Mazza, M. Ilchen, A. J. Rafipoor, C. Callegari, P. Finetti, O. Plekan, K. C. Prince, R. Richter, M. B. Danailov, A. Demidovich, G. De Ninno, C. Grazioli, R. Ivanov, N. Mahne, L. Raimondi, C. Svetina, L. Avaldi, P. Bolognesi, M. Coreno, P. O’Keeffe, M. Di Fraia, M. Devetta, Y. Ovcharenko, Th. Möller, V. Lyamayev, F. Stienkemeier, S. Dusterer, K. Ueda, J. T. Costello, A. K. Kazansky, N. M. Kabachnik, and M. Meyer, *Nature Communications* **5** (2014) 4648.
- [17] L. Giannessi, E. Allaria, K. C. Prince, C. Callegari, G. Sansone, K. Ueda, T. Morishita, Chien Nan Liu, A. N. Grum-Grzhimailo, E. V. Gryzlova, N. Douguet, and K. Bartschat, *Scientific Reports* **8** (2018) 7774.
- [18] C. Spezzani, E. Allaria, M. Coreno, B. Diviacco, E. Ferrari, G. Geloni, E. Karantzoulis, B. Mahieu, M. Vento, and G. De Ninno, *Phys. Rev. Lett.* **107** (2011) 084801.
- [19] M. Ilchen, N. Douguet, T. Mazza, A. J. Rafipoor, C. Callegari, P. Finetti, O. Plekan, K. C. Prince, A. Demidovich, C. Grazioli, L. Avaldi, P. Bolognesi, M. Coreno, M. Di Fraia, M. Devetta, Y. Ovcharenko, S. Dusterer, K. Ueda, K. Bartschat, A. N. Grum-Grzhimailo, A. V. Bozhevolnov, A. K. Kazansky, N. M. Kabachnik, and M. Meyer *Phys. Rev. Lett.* **118** (2017) 013002.
- [20] N. Douguet, A. N. Grum-Grzhimailo, E. V. Gryzlova, E. I. Staroselskaya, J. Venzke, and K. Bartschat, *Phys. Rev. A* **93** (2016) 033402.
- [21] G. Mainfray and C. Manus, *Rep. Prog. Phys.* **54** (1991) 1333.
- [22] J. H. Eberly, J. Javanainen, K. Rzażewski, *Phys. Reports* **204** (1991) 331.
- [23] R. Freeman, P. Bucksbaum, W. Cooke, G. Gibson, T. McIlrath, and L. van Woerkom, in: M. Gavrilu (ed.), *Atoms in Intense Laser Fields* (Academic Press, New York, 1992), p. 43.
- [24] B. Sheehy and L. F. DiMauro, *Annu. Rev. Phys. Chem.* **47** (1996) 463.
- [25] M. V. Fedorov, *Atomic And Free Electrons In A Strong Light Field* (World Scientific Singapore, 1997).
- [26] N. B. Delone and V. P. Krainov, *Multiphoton Processes in Atoms* (Springer, Berlin, 2000).
- [27] C. J. Joachain, N. J. Kylstra, and R. M. Potvliege, *Atoms in Intense Laser Fields* (Cambridge University Press, Cambridge, UK, 2012).
- [28] V. Tagliamonti, P. Sándor, A. Zhao, T. Rozgonyi, P. Marquetand, and T. Weinacht, *Phys. Rev. A* **93** (2016) 051401(R).
- [29] N. A. Hart, J. Strohaber, A. A. Kolomenskii, G. G. Paulus, D. Bauer, and H. A. Schuessler, *Phys. Rev. A* **93** (2016) 063426.
- [30] A. Bunjac, D. B. Popović, and N. S. Simonović, *Phys. Chem. Chem. Phys.* **19** (2017) 19829.
- [31] R. R. Freeman, P. H. Bucksbaum, H. Milchberg, S. Darack, D. Schumacher, and M. E. Geusic, *Phys. Rev. Lett.* **59** (1987) 1092.
- [32] J. L. Madajczyk, M. Pont, R. M. Potvliege, R. Shakeshaft, H. S. Taylor, *Phys. Rev. A* **45** (1992) 4848.
- [33] R. M. Potvliege, *Comp. Phys. Commun.* **114** (1998) 42.
- [34] M. Crance, *J. Opt. Soc. Am. B* **7** (1990) 449.
- [35] M. Dörr, R. M. Potvliege, R. Shakeshaft, *Phys. Rev. A* **41** (1990) 558.
- [36] S. Vučić, *J. Phys. B* **45** (2012) 185601.
- [37] J. H. Eberly and J. Javanainen, *Phys. Rev. Lett.* **60** (1988) 1346.
- [38] V. I. Ritus, *Zh. Eksp. Teor. Fiz.* **51** (1966) 1544. [*Sov. Phys. JETP* **24** (1967) 1041].
- [39] A. A. Krylovetsky, N. L. Manakov, and S. I. Marmo, *Laser Physics* **7** (1997) 781.